The Astrophysical Journal Letters, 753:L29 (7pp), 2012 July 10 doi:10.1088/2041-8205/753/2/L29

AN EXTREME ULTRAVIOLET WAVE ASSOCIATED WITH A MICRO-SIGMOID ERUPTION

Ruisheng Zheng, Yunchun Jiang, Jiayan Yang, Yi Bi, Junchao Hong, Dan Yang, and Bo Yang
National Astronomical Observatories/Yunnan Astronomical Observatory, Chinese Academy of Sciences, Kunming 650011, China; zhrsh@ynao.ac.cn
Received 2012 May 12; accepted 2012 May 29; published 2012 June 19

ABSTRACT

Taking advantage of the high temporal and spatial resolution of the *Solar Dynamics Observatory* (*SDO*) observations, we present an extreme ultraviolet (EUV) wave associated with a micro-sigmoid eruption on 2010 October 21. The micro-sigmoid underwent a typical "sigmoid-to-arcade" evolution via tether-cutting reconnection, accompanied by a B1.7 flare, a filament eruption, and coronal twin dimmings. In the eruption, the newly formed sigmoidal loops expanded quickly, and the expansion likely triggered an EUV wave. The wave onset was nearly simultaneous with the start of the eruption and the associated flare. The wave had a nearly circular front and propagated at a constant velocity of 270–350 km s^{-1} with very little angular dependence. Remarkably, in some direction, the wave encountered a small loop and refracted at a higher speed. All the results provide evidences that the wave was a fast-mode magnetohydrodynamic (MHD) wave. Owing to the close temporal and spatial relationship between the wave and the expanding loops, we believe that the wave was most likely triggered by the fast expansion of the newly formed sigmoidal loops, which evolved into the leading front of the invisible micro-coronal mass ejection.

Key words: Sun: activity – Sun: corona – Sun: filaments, prominences

Online-only material: color figures

1. INTRODUCTION

Extreme ultraviolet (EUV) waves, first observed by the EUV Imaging Telescope (EIT) on board the *Solar and Heliospheric Observatory* (*SOHO*) spacecraft (e.g., Moses et al. 1997; Thompson et al. 1998), have been an active research topic in solar physics. EUV waves generally appear as large-scale, diffuse, single-pulse coronal-enhanced transients. They normally emanate from flaring and eruptive active regions (ARs), and subsequently propagate over significant fractions of the solar disk, mostly over quiet-Sun areas. Their speeds can reach several hundred km s^{-1} (Thompson & Myers 2009). EUV waves tend to avoid ARs and the separatrix betweens ARs. They reflect or refract at the boundaries of coronal holes or near coronal loops (Thompson et al. 1998, 1999; Wills-Davey & Thompson 1999; Wu et al. 2001; Li et al. 2012). More and more evidences demonstrate that EUV waves are intimately associated with coronal mass ejections (CMEs; or other types of mass motions) rather than flares (Biesecker et al. 2002; Cliver et al. 2005; Chen 2006; Zheng et al. 2012).

The physical nature of EUV waves has been strongly debated. There are some competing models, such as coronal fast-mode magnetohydrodynamic (MHD) waves (e.g., Thompson et al. 1999; Wang 2000; Wu et al. 2001; Ofman & Thompson 2002; Long et al. 2008; Gopalswamy et al. 2009; Veronig et al. 2010), slow-mode or soliton-like waves (Wills-Davey et al. 2007; Wang et al. 2009), pseudowaves related to a current shell or successive restructuring of magnetic field associated with the CME expansion (Delannée et al. 2008; Attrill et al. 2007), and hybrid models including both wave and pseudowave scenarios (Chen et al. 2002; Zhukov & Auchère 2004; Cohen et al. 2009; Downs et al. 2011; Cheng et al. 2012). For details of observations and models, please refer to recent reviews (Wills-Davey & Attrill 2009; Gallagher & Long 2011; Warmuth 2010; Zhukov 2011; Patsourakos & Vourlidas 2012).

Sigmoids, first investigated by Rust & Kumar (1996), are often composed of two opposite J-like bundles of loops (Canfield et al. 2007; McKenzie & Canfield 2008). These are forward or inverse S-shaped coronal loops seen mainly in soft X-rays and sometimes in EUV (Liu et al. 2007, 2010). The sigmoid eruption usually undergo a process termed "sigmoid-to-arcade" evolution (Sterling et al. 2000; Moore et al. 2001; Pevtsov 2002; Gibson et al. 2002). It is generally accepted that the sigmoidal ARs have a higher possibility of eruption to produce the associated flares and CMEs (Hudson et al. 1998; Canfield et al. 1999; Glover et al. 2000). Thus, the sigmoid is now regarded as an important precursor of a CME and an important signature in space weather forecasts (Canfield et al. 2000; Rust et al. 2005). To date, most of the observed sigmoids are large scale, and micro-sigmoids are very rare (Mandrini et al. 2005; Raouafi et al. 2010). Moreover, the sigmoid eruptions are primarily associated with CMEs, flares, and filament eruptions. To our knowledge, the sigmoid eruption associated with an EUV wave is only studied in one event (Ma et al. 2009).

In this Letter, with the high-cadence and sensitivity observations from the Helioseismic and Magnetic Imager (HMI) and Atmospheric Imaging Assembly (AIA; Lemen et al. 2012) both on the *Solar Dynamics Observatory* (*SDO*; Pesnell et al. 2012), we concentrate on an EUV wave associated with a micro-sigmoid eruption on 2010 October 21.

2. OBSERVATIONS AND DATA ANALYSIS

On 2010 October 21, a small EUV wave emanated from a small AR in S06E32 of the solar disk. It was associated with a micro-sigmoid eruption, a B1.7 flare. There is no visible filament in the Hα filtergrams and no detectable CME in the coronagraphs. The eruption center is identified at the location of $x = -525''$, $y = -175''$, measured from the solar disk center. We mainly use the observations from the AIA on the *SDO*. The AIA has 10 EUV and UV wavelengths, covering a wide range of temperatures. The cadence is up to 12 s, and the pixel resolution is $0''.6$. The wave is best seen in 211 Å. In order to analyze the dynamics of the waves, we employ a time-slice approach in which the slices start from the identified eruption center and had a length of $500''$. In addition, magnetograms from the HMI

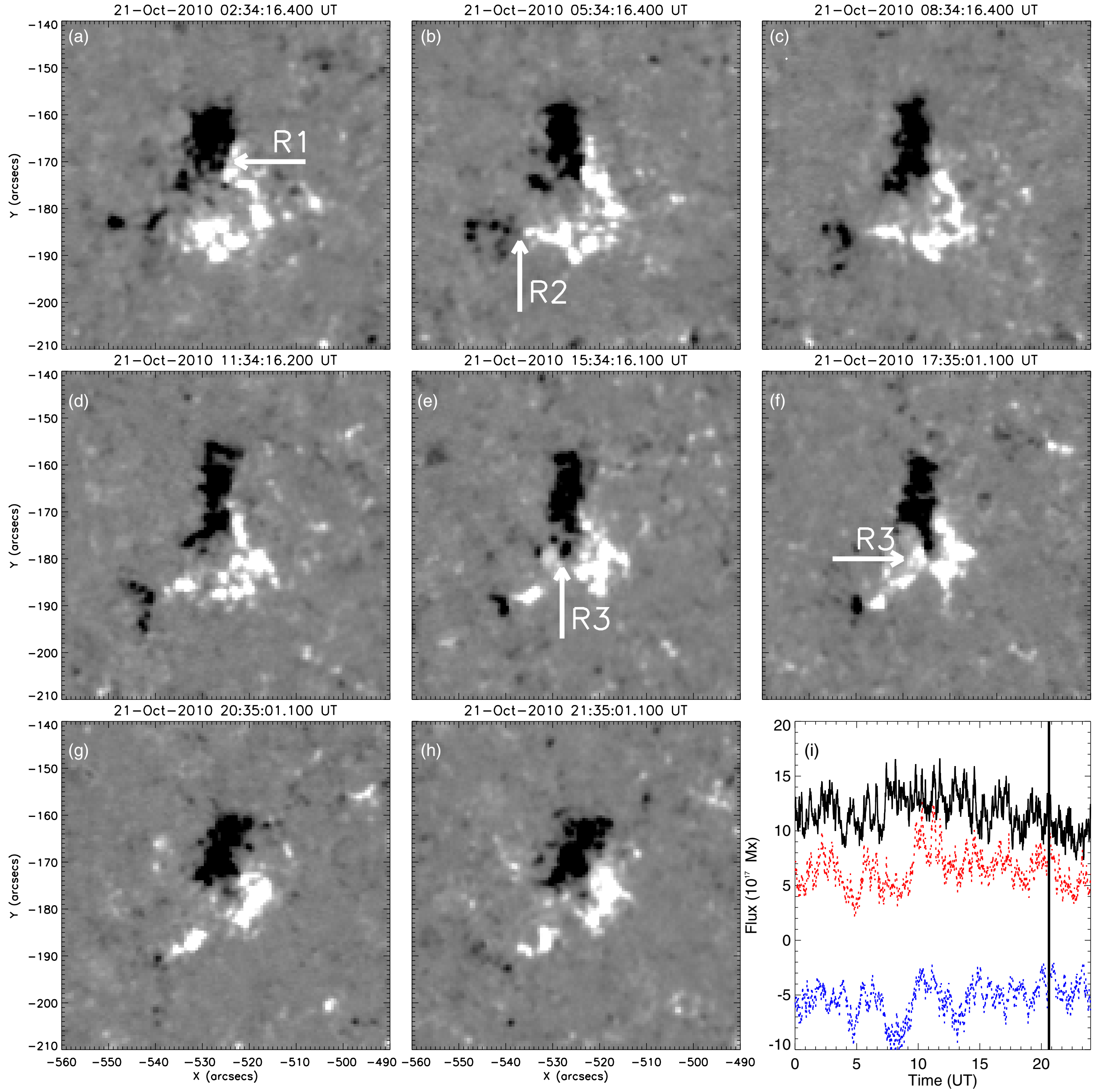

Figure 1. General appearance of the source AR in HMI magnetograms (panels (a)–(h)) and the magnetic flux evolution (panel (i)) for the whole AR. R1–R3 are the main cancellation regions. The vertical line in panel (i) points out the eruption time.

(A color version of this figure is available in the online journal.)

are chosen to check the magnetic field evolution of the eruption region. All the images are differentially rotated to a reference time (∼20:30:00 UT).

3. RESULTS

3.1. Magnetic Activities

The general appearance of the small AR is shown by HMI magnetograms in Figure 1. The AR had a bipolar magnetic morphology (panel (a)), which consisted of a leading positive-polarity sunspot and a following negative-polarity sunspot. The leading sunspot was diffuse. For the following sunspot, the northern part was compact and strong, and the southern part was faint and weak. So, the polarity inversion line (PIL) was indistinct, and only the north was clear. Prior to the eruption, the magnetic field in the source region was very active. The magnetic flux cancellation occurred near the PIL, mainly at regions R1 and R2 (the arrows in panels (a) and (b)). There was also the magnetic flux emergence in the course of evolution for the magnetic field. The cancellation region R3 (arrows in panels (e) and (f)) was possibly formed as a result of the emergence. Because of the continuous emergence and cancellation, the southern part of the following sunspot had almost disappeared some minutes before the eruption (panel (g)). After the eruption, the emergence and cancellation continued (panel (h)). The changes of the magnetic fluxes for the whole AR are plotted

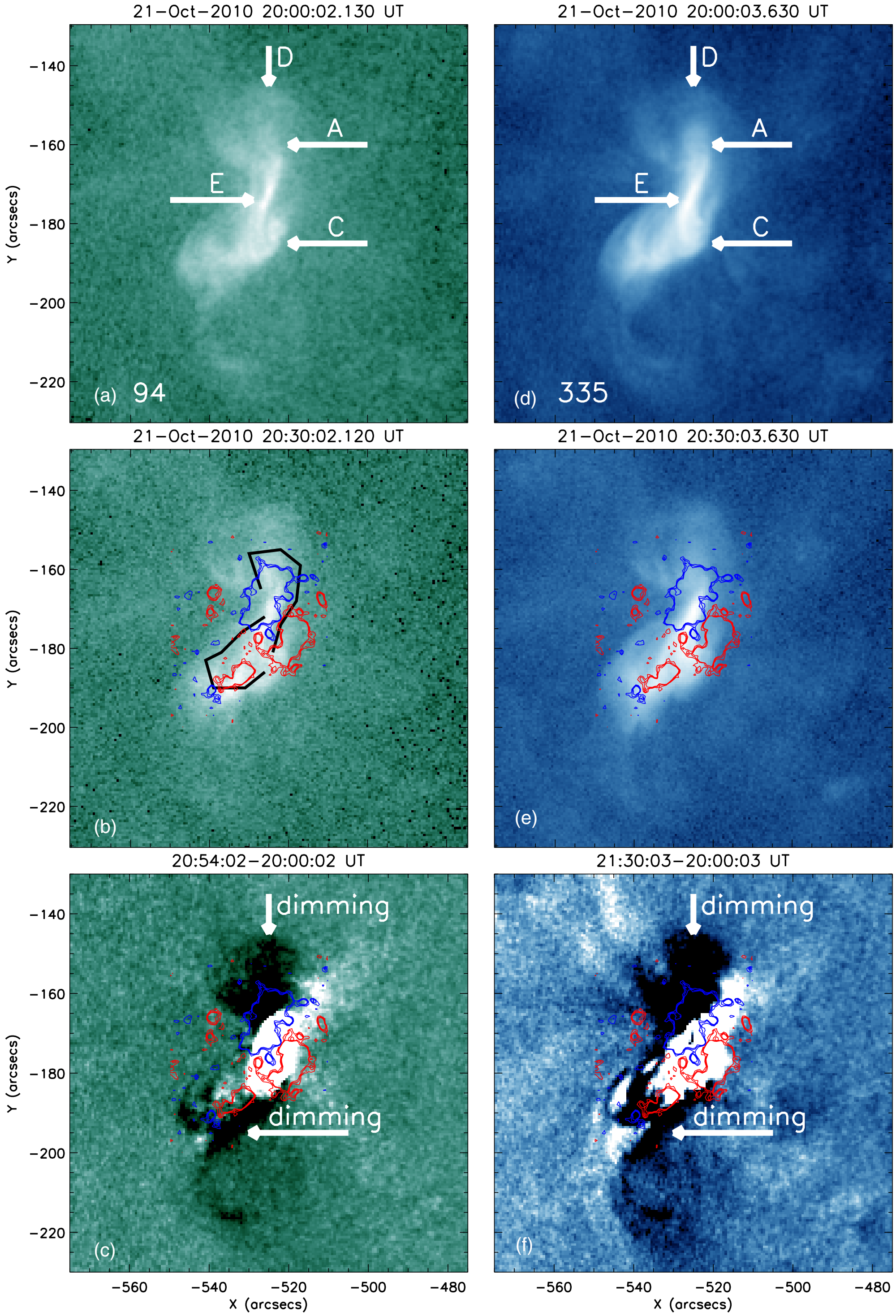

Figure 2. Sigmoid eruption in the AIA 94 Å (left panels) and 335 Å (right panels) images. A–E denote the associated structures in the Moore's model for the sigmoid eruption. Contours of HMI longitudinal magnetic fields at 20:30:31 UT are superposed on the middle and bottom panels with positive (negative) fields in red (blue). The levels are 20, 30, and 40 G, respectively. The curved black lines in panel (b) sketch the profiles of the sigmoid elbows.

(A color version of this figure is available in the online journal.)

in panel (i) in which the vertical line marks the onset of the eruption (about 20:37 UT). For both polarity fluxes, the plots show strong fluctuations and have a tendency to decline the entire day, consistent with the continuous emergence and cancellation. We believe that there was a close relation between the eruption and the continuous magnetic activities in the source region.

3.2. Micro-sigmoid Eruption

Figure 2 shows the sigmoid eruption in the AIA 94 Å (left panels) and 335 Å (right panels) images. The sigmoid only had a length of 50″, which was approximately one-fifth the size of the large-scale sigmoid studied by McKenzie & Canfield (2008). Thus, it could be regarded as a micro-sigmoid (Raouafi

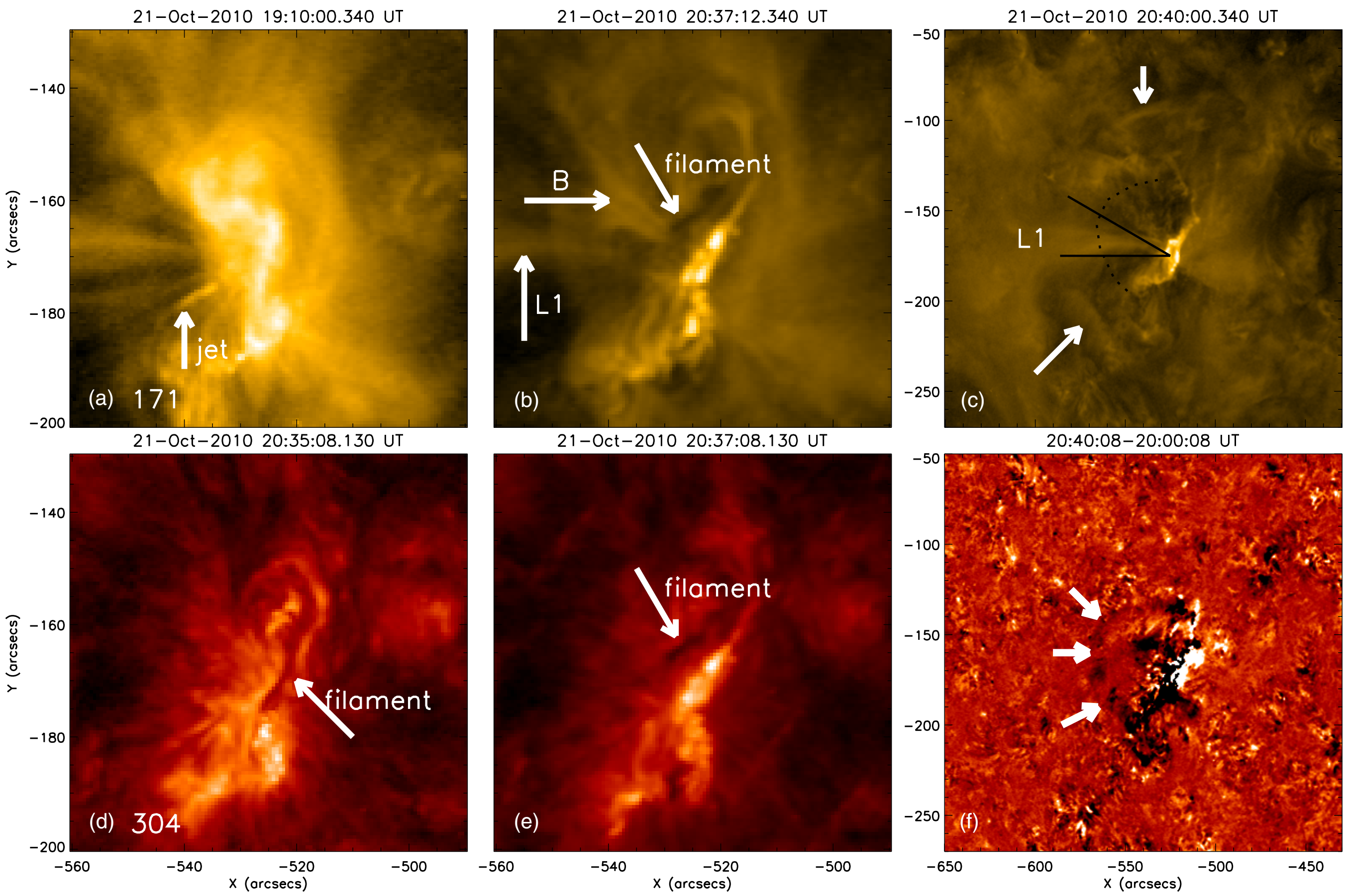

Figure 3. Associated features for the sigmoid eruption in the AIA 171 Å (upper panels) and 304 Å (bottom panels) images. In panel (c), the arrows indicate the expanding loops (D), and the solid lines measure the distances from the eruption center to D. In panel (f), the arrows point out the eruptive filament that is shown by the dotted line in panel (c).

(A color version of this figure is available in the online journal.)

et al. 2010). In panels (a) and (d), following the nomenclature in Moore's sigmoid model (Moore et al. 2001), the two oppositely curved magnetic elbows were marked as A and C. It was a pity that the envelope loops in theory were invisible here. The continuous magnetic flux cancellation near the eruption center resulted in the reconnection between two elbows, same as the tether-cutting reconnection in Moore's model (Moore et al. 2001; Liu et al. 2010). According to the model, the reconnection produced the low-lying sheared compact loops (E) under the middle of the sigmoid and the new sigmoidal loops (D). Before the eruption, only part of the elbows reconnected, so the elbows and the newly formed loops could coexist. Superposed with the contours of the HMI magnetic field and the profiles of elbows, the four footpoints were rooted at the two opposite polarities of the bipolar AR (panels (b) and (e)). At about 02:36 UT, the sigmoid began to erupt and was accompanied by a B1.7 flare. Owing to the strong intensity, the evolution in the core field was covered by the brightness. After the eruption, there appeared a post-eruption arcade straddling the middle of the PIL (panels (c) and (f)). It was compatible with the typical sigmoid-to-arcade evolution. The arcade was not like the cusp structure in the soft X-ray (Sterling et al. 2000; Moore et al. 2001). Of course, there were the distinct twin dimmings around the arcade, another product of a typical sigmoid eruption, rooted at opposite magnetic polarities.

The eruption is shown in detail by the images of AIA 171 and 304 Å in Figure 3. Prior to the eruption, several jets were ejected from the center of the sigmoid (panel (a)), consistent with the tether-cutting model. Because the continuous magnetic activities made the eruption region very bright, many of the small jets could not be distinguished. The envelope loops (B) predicted by Moore et al. (2001) were very obvious in 171 Å (panel (b)). The north end of B was indicated by the arrow, but the south end merged in the ambient loops. Note that there was another loop (L1 in panel (b)) near B. There was no visible filament in the Hα filtergrams, but some minutes before the eruption, there clearly appeared a small filament in the eruption center (panel (d)). We suggest that the small filament was covered by the overlying bright structure (e.g., D) before the eruption and began to emerge until the rising of the overlying structure. Following the rising of D, the filament was slowly rising (panels (b) and (e)) and the envelope loops (B) were pushed upward. At about 20:40 UT, the ends of B had disappeared and the expansion of D was very clear (arrows in panel (c)). At the same time, the erupting filament had expanded as an arcade (arrows in panel (f) and the dotted curved line in panel (c)). Interestingly, L1 was nearly intact during the eruption, likely because they did not overlie the sigmoid.

The evolution of the dimmings is shown in AIA 211, 193, 171, and 131 Å in Figure 4. The pre-eruption images (left panels) are overlaid with the intensity counter of the image in Figure 2(a). The sigmoid was obvious in 211 and 193 Å (panels (a) and (c)). The 171 and 131 Å images did not show the sigmoid clearly, but revealed the ambient loops (panels (e) and (g)) better. After the

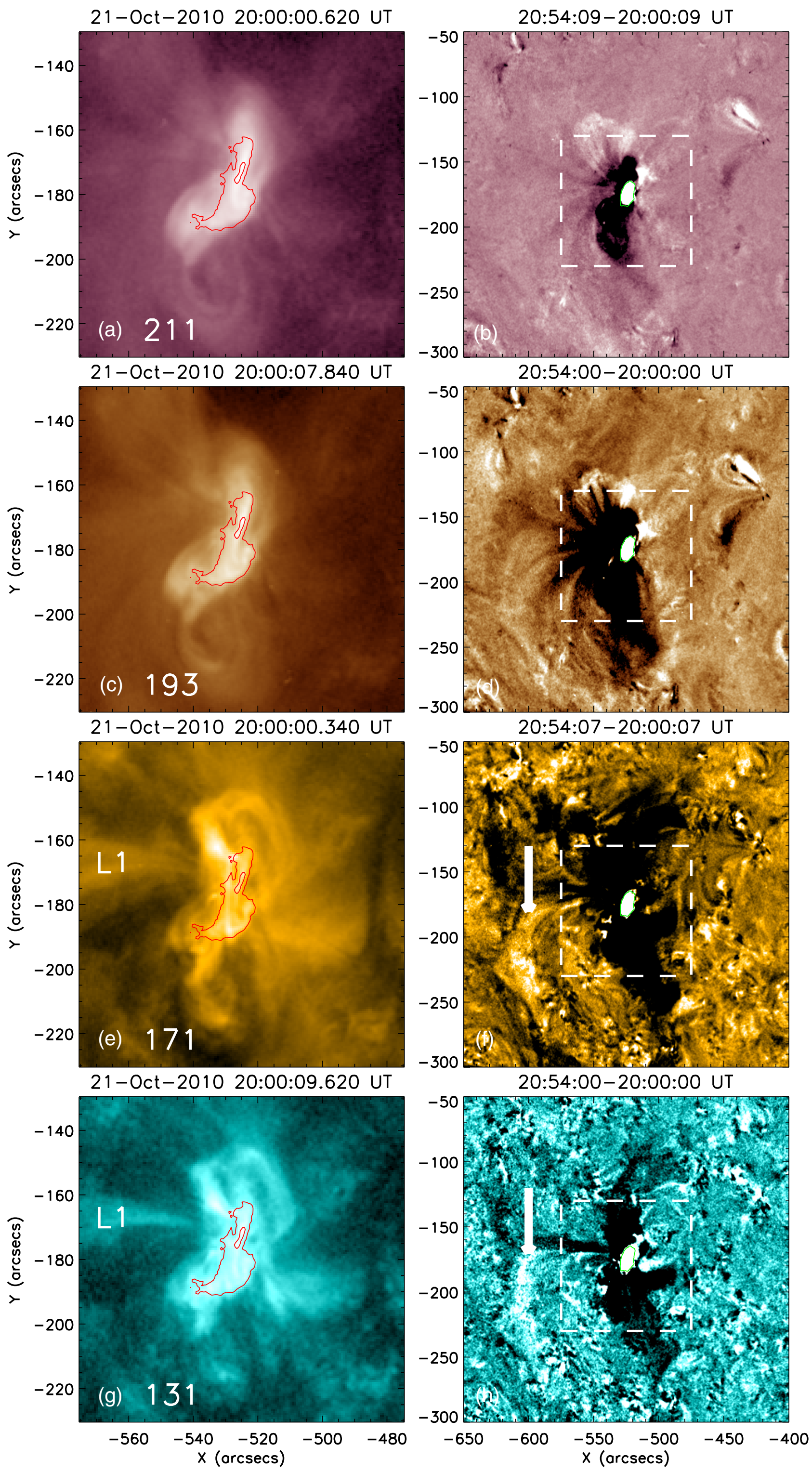

Figure 4. Coronal dimmings in the AIA 211, 193, 171, and 131 Å images. The images in the left panels are overlaid by the intensity counter (red) of the image in Figure 2(a), and the images in the right panels are overlaid by the 10% intensity contour (green) of the AIA 94 Å image at 02:54:02 UT. The field of view (FOV) of the left panels is indicated by the dashed boxes in the right panels, and the arrows in panels (f) and (h) point to the intact loops (L1) in the eruption.

(A color version of this figure is available in the online journal.)

eruption, only the post-eruption arcade over the eruption center in the four wavelengths (right panels) was left. Overlaid by the 10% intensity contour of the AIA 94 Å image at 02:54:02 UT, we noted that the post-eruption arcade in these different wavelengths was nearly cospatial. Around the arcade, the twin deep dimmings were more obvious, especially in 171 Å, likely attributed to the loop disruption during the sigmoid eruption. The dimmings appeared in many wavelengths that had a wider temperature, which could be interpreted as the depletion of the coronal material. Moreover, the twin dimmings were not transient, but sustained for several hours. The long-duration deep dimmings could be treated as the indicator of the CME. In

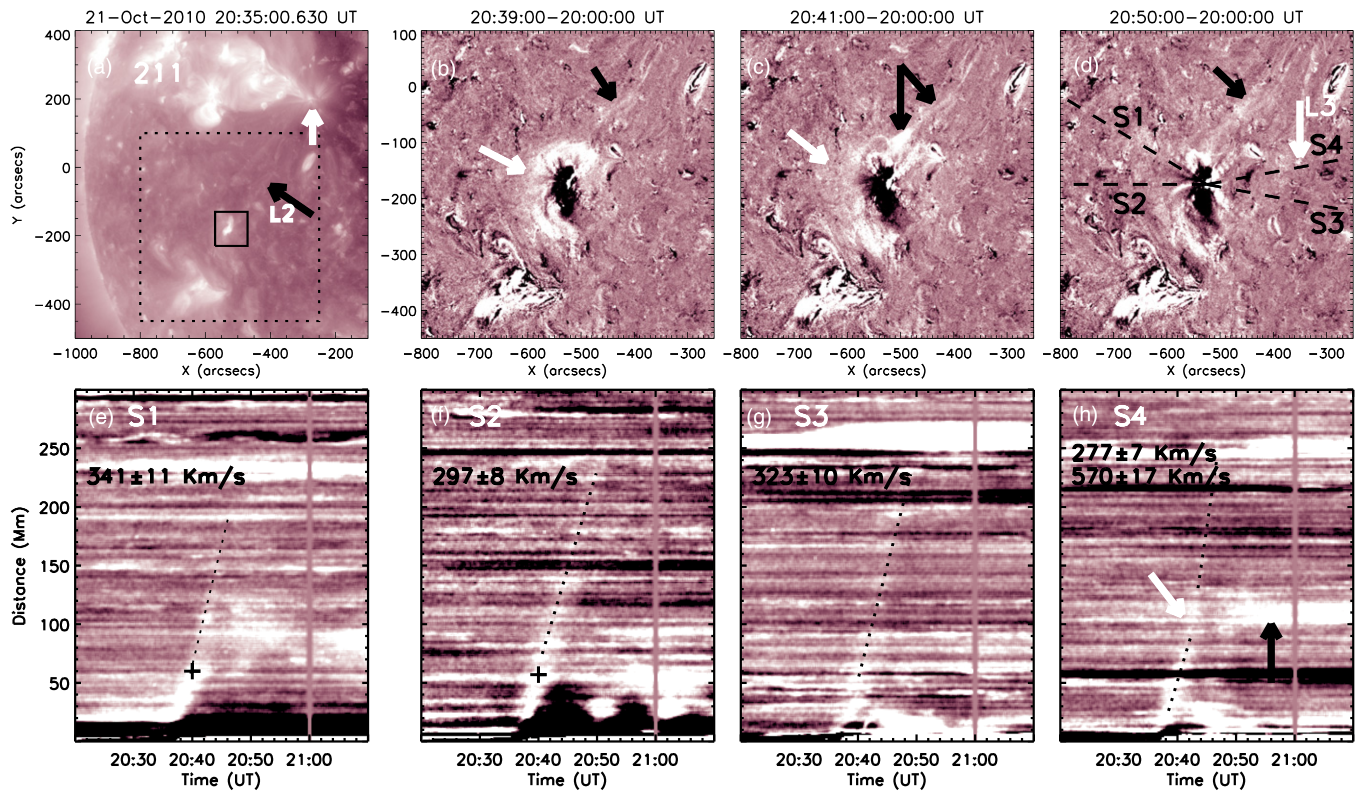

Figure 5. Original (panel (a)) and base difference images (panels (b)–(d)) in AIA 211 Å displaying the evolution of the wave, and base difference time-slice images (bottom panels) along the sectors S1–S4 (dashed lines in panel (d)). In panel (a), the small solid box shows the sigmoid region, and the big dotted box indicates the FOV of panels (b)–(d). The AR connects the magnetic separatrix (the white arrow in panel (a)) with the long loops (L2), indicated by black arrows in the upper panels. The white arrows in panels (b) and (c) point out the wave front, and those in panels (d) and (i) denote the small loops (L3). The black arrow in panel (i) indicates the brightening of L3. Wave fronts are indicated by dotted lines, with the linear fitted velocities attached above. The plus symbols in panels (e) and (f) indicate the locations of the wave front at 20:40 UT in S1 and S2.

(A color version of this figure is available in the online journal.)

addition, the surviving L1 is indicated by the arrows in panels (f) and (h).

3.3. EUV Wave

The sigmoid eruption was closely associated with an EUV wave, which is shown in AIA 211 Å in Figure 5. Panel (a) exhibits the general view of the eruption environment. The micro-sigmoid is located at the quiet region (the solid box), far away from the nearest AR in the southeast. It was notable that there were some large long loops (L2, indicated by the black arrow) in the northwest of the AR, connecting the magnetic separatrix (the white arrow) farther northeast. The wave was weak and small, and the propagation distance was less than 300 Mm. But the wave had a nearly circular front, which was pointed by white arrows in panels (b) and (c). It was remarkable that, during the wave propagation, L2 became brighter due to wave compression rather than became disrupted (black arrows in panels (b)–(d)).

To best display the kinematics of the EUV wave, we employ the time-slice approach and analyze the evolution of the wave front along the selected slices (S1-S4). The angles of S1-S4 are 60°, 90°, 260°, and 280°, respectively, counted counterclockwise from the north (black dashed lines in panel (d)).

The bottom panels of Figure 5 display the propagation of the wave in S1–S4. The wave set off at about 20:37 UT, almost simultaneous with the onset of the sigmoid eruption and the associated flare. The wave front appeared as bright oblique stripes, denoted by the black dotted lines. The wave was most obvious and propagated up to a distance of about 250 Mm. The following speeds and associated errors were derived by linear fits, assuming that the measurement uncertainty of the selected points is 4 pixel (∼1.74 Mm). In S1–S3, the wave nearly propagated at constant velocities, and the speeds were 341 ± 11, 297 ± 8, and 323 ± 10 km s^{-1}, respectively. Intriguingly, the wave in S4 refracted at the site about 100 Mm far from the eruption center (indicated by the white arrow), corresponding to a small loop (L3, indicated by the white arrow in panel (d)). The incident speed was 277 ± 7 km s^{-1}, and the refracted speed was 570 ± 17 km s^{-1}. The L3 became very bright (the black arrow in panel (h)) after the wave pass, suggesting that L3 was activated by the wave.

4. DISCUSSION AND CONCLUSIONS

In general, a sigmoid is an important precursor of a CME (Canfield et al. 2000), and a successful sigmoid eruption likely produced a CME, following Moore's model (Moore et al. 2001). However, we do not find any CME associated with the sigmoid eruption in any coronagraph. The coronal dimmings are an important signature of CMEs. Thus, the long-duration deep dimmings and the observable eruptive filament likely can demonstrate the existence of the associated CME. The weak intensity or the small extent of the CME could have resulted in its escape from detection. Furthermore, the eruption of the micro-sigmoid likely gave rise to the micro-CME (Raouafi et al. 2010) that is hardly seen.

Micro-sigmoids are very unusual and have only been studied in a few events. Limited by the lower resolution of the previous observations, micro-sigmoids are always in the form of X-ray bright points. Mandrini et al. (2005) first observed a micro-sigmoid (∼80″) eruption mainly in EUV and provided evidence that the eruption was linked to the smallest interplanetary magnetic cloud then. Using *Hinode*/XRT images, Raouafi et al. (2010) studied many micro-sigmoids (∼30–50″) at the polar coronal holes and suggested that coronal micro-sigmoids may well be progenitors of coronal jets. However, none of the micro-sigmoid eruptions in the above examples are associated with EUV waves. Ma et al. (2009) observed an EUV wave associated with a sigmoid eruption, but the sigmoid was about 200″ in length, much larger than micro-sigmoids. Combining with the high-quality observations from the HMI and AIA on the *SDO*, we first analyzed a micro-sigmoid (∼50″) eruption that was associated with an EUV wave on 2010 October 21.

Our main findings are as follows. (1) In the source region, the continuous emergence and cancellation of the magnetic flux led to the tether-cutting reconnection of the micro-sigmoid. (2) The micro-sigmoid eruption underwent the typical sigmoid-to-arcade transition and was accompanied by a B1.7 flare, a small filament eruption, an invisible micro-CME, and twin dimmings. (3) The micro-sigmoid eruption was closely associated with an EUV wave. The wave onset was nearly simultaneous with the onset of the sigmoid eruption and the flare. (4) The wave had a nearly circular front and propagated at constant velocities of 270–350 km s^{-1} with very little angular dependence, which was in the range of the average surface-projected expansion speeds for fast-mode waves (Wang 2000). Particularly, in some directions, the wave encountered a small loop and refracted at a higher speed. All results provide evidences that the EUV wave was a fast-mode MHD wave.

As to the physical origin of the wave, the analysis is as follows. It is widely accepted that EUV waves are intimately associated with CMEs rather than flares (Biesecker et al. 2002; Cliver et al. 2005; Chen 2006). Though the onset of the wave was almost simultaneous with the start of the B1.7 flare, the weak intensity decreased the possibility that the flare induced the wave. The associated micro-CME was invisible, but the expansion of the newly formed sigmoidal loops (D) were very clear, which finally evolved into the leading front of the CME. In S1 and S2, at about 20:40 UT, the distances from D to the eruption center are about 47 and 44 Mm (black straight lines in Figure 3(c)), respectively, and the wave fronts are about 60 and 56 Mm far from the eruption center, respectively. Owing to the close temporal and spatial relationship between the wave and the expanding loops, we believe that the wave was most likely triggered by the fast expansion of the newly formed sigmoidal loops (D), i.e., the leading front of the associated CME.

However, it is somewhat puzzling that the eruption condition for the micro-sigmoid can trigger an EUV wave. In addition, we need to think what special loop can refract the wave, but not other loops. These make the wave nature uncertain and leave other possibilities open. More studies of this kind of wave will be helpful in understanding their nature and the relation with associated eruptions. The nature and origin of EUV waves remain subtle; further observations and theoretical work will be essential.

The authors thank the *SDO* team for providing the excellent data. This work is supported by the 973 Program (2011CB811403) and by the Natural Science Foundation of China under grants 10973038, 11173058, and 11103090. The authors thank the anonymous referee for constructive comments.

REFERENCES

Attrill, G. D. R., Harra, L. K., van Driel-Gesztelyi, L., & Démoulin, P. 2007, ApJ, 656, L101
Biesecker, D. A., Myers, D. C., Thompson, B. J., et al. 2002, ApJ, 569, 1009
Canfield, R. C., Hudson, H. S., & McKenzie, D. E. 1999, Geophys. Res. Lett., 26, 627
Canfield, R. C., Hudson, H. S., & Pevtsov, A. A. 2000, IEEE Trans. Plasma Sci., 28, 1786
Canfield, R. C., Kazachenko, M. D., Acton, L. W., et al. 2007, ApJ, 671, L81
Chen, P. F. 2006, ApJ, 641, L153
Chen, P. F., Wu, S. T., Shibata, K., & Fang, C. 2002, ApJ, 572, L99
Cheng, X., Zhang, J., Olmedo, O., et al. 2012, ApJ, 745, L5
Cohen, O., Attrill, G. D. R., Manchester, W. B., IV, & Wills-Davey, M. J. 2009, ApJ, 705, 587
Cliver, E. W., Laurenza, M., Storini, M., & Thompson, B. J. 2005, ApJ, 631, 604
Delannée, C., Török, T., Aulanier, G., & Hochedez, J. F. 2008, Sol. Phys., 247, 123
Downs, C., Roussev, I. I., van der Holst, B., et al. 2011, ApJ, 728, 2
Gallagher, P. T., & Long, D. M. 2011, Space Sci. Rev., 158, 365
Gibson, S. E., Fletcher, L., Del Zanna, G., et al. 2002, ApJ, 574, 1021
Glover, A., Ranns, N. D. R., Harra, L. K., & Culhane, J. L. 2000, Geophys. Res. Lett., 27, 2161
Gopalswamy, N., Yashiro, S., Temmer, M., et al. 2009, ApJ, 691, L123
Hudson, H. S., Lemen, J. R., St. Cyr, O. C., Sterling, A. C., & Webb, D. F. 1998, Geophys. Res. Lett., 25, 2481
Lemen, J. R., Title, A. M., Akin, D. J., et al. 2012, Sol. Phys., 275, 17
Li, T., Zhang, J., Yang, S. H., & Liu, W. 2012, ApJ, 746, 13
Liu, C., Lee, J., Yurchyshyn, V., et al. 2007, ApJ, 669, 1372
Liu, R., Liu, C., Wang, S., Deng, N., & Wang, H. M. 2010, ApJ, 725, L84
Long, D. M., Gallagher, P. T., McAteer, R. T. J., & Bloomfield, D. S. 2008, ApJ, 680, L81
Ma, S., Wills-Davey, M. J., Lin, J., et al. 2009, ApJ, 707, 503
Mandrini, C. H., Pohjolainen, S., Dasso, S., et al. 2005, A&A, 434, 725
McKenzie, D. E., & Canfield, R. C. 2008, A&A, 481, L65
Moore, R. L., Sterling, A. C., Hudson, H. S., & Lemen, J. R. 2001, ApJ, 532, 833
Moses, D., Clette, F., Delaboudinière, J.-P., et al. 1997, Sol. Phys., 175, 571
Ofman, L., & Thompson, B. J. 2002, ApJ, 574, 440
Patsourakos, S., & Vourlidas, A. 2012, Sol. Phys., in press
Pesnell, W. D., Thompson, B. T., & Chamberlin, P. C. 2012, Sol. Phys., 275, 3
Pevtsov, A. A. 2002, Sol. Phys., 207, 111
Raouafi, N.-E., Georgoulis, M. K., Rust, D. M., & Bernasconi, P. N. 2010, ApJ, 718, 981
Rust, D. M., Georgoulis, M. K., Bernasconi, P. N., & LaBonte, B. J. 2005, Johns Hopkins APL Tech. Dig., 26, 123
Rust, D. M., & Kumar, A. 1996, ApJ, 464, L199
Sterling, A. C., Hudson, H. S., Thompson, B. J., & Zarro, D. M. 2000, ApJ, 532, 628
Thompson, B. J., Gurman, J. B., Neupert, W. M., et al. 1999, ApJ, 517, L151
Thompson, B. J., & Myers, D. C. 2009, ApJS, 183, 225
Thompson, B. J., Plunkett, S. P., Gurman, J. B., et al. 1998, Geophys. Res. Lett., 25, 2465
Veronig, A. M., Muhr, N., Kienreich, I. W., Temmer, M., & Vršnak, B. 2010, ApJ, 716, L157
Wang, H., Shen, C., & Lin, J. 2009, ApJ, 700, 1716
Wang, Y. M. 2000, ApJ, 543, L89
Warmuth, A. 2010, Adv. Space Res., 45, 527
Wills-Davey, M. J., & Attrill, G. D. R. 2009, Space Sci. Rev., 149, 325
Wills-Davey, M. J., DeForest, C. E., & Stenflo, J. O. 2007, ApJ, 664, 556
Wills-Davey, M. J., & Thompson, B. J. 1999, Sol. Phys., 190, 467
Wu, S. T., Zheng, H. N., Wang, S., et al. 2001, J. Geophys. Res., 106, 25089
Zheng, R. S., Jiang, Y. C., Yang, J. Y., et al. 2012, ApJ, 747, 67
Zhukov, A. N. 2011, J. Atmos. Sol.-Terr. Phys., 73, 1096
Zhukov, A. N., & Auchère, F. 2004, A&A, 427, 705